CFD-DEM modeling of seepage erosion around shield tunnels

Dong-Mei ZHANG[1,*], Cheng-Peng GAO[1] and Zhen-Yu YIN[2*]

Affiliations:

[1] Key Laboratory of Geotechnical and Underground Engineering of Ministry of Education; Department of Geotechnical Engineering, College of Civil Engineering, Tongji University, Shanghai, China, 200092

[2] Department of Civil and Environmental Engineering, The Hong Kong Polytechnic University, Hung Hom, Kowloon, Hong Kong

[*] Corresponding authors: E-mail addresses: dmzhang@tongji.edu.cn (D.M. Zhang), zhenyu.yin@polyu.edu.hk; zhenyu.yin@gmail.com (Z.Y. Yin).

Abstract: When tunnels are built in saturated silty sand, the tunnel leakage can carry fine particles into tunnels and generate seepage erosion process. During this process sand particles are subjected to high confining and hydraulic pressures and then are eroded through the seams of segmental joints. This paper investigates the mechanism of seepage erosion process using Computational Fluid Dynamics and Discrete Element Method (CFD-DEM) coupling simulations. The seepage erosion processes are simulated for loose, medium dense and dense silty sand, respectively. The evolution of the fine particles loss and the volumetric strain are investigated. Results show that the fine particles are eroded in two patterns. The first pattern is induced by axial pressure extruding fine particles through seams without hydraulic pressure. The second pattern is induced by fluid drag force dragging fine particles under hydraulic pressure. Correspondingly, the erosion process is divided into two stages as initial extruding stage and the following eroding stage. Result shows that dense sand is more prone to particle erosion in the first pattern while loose sand are gradually more prone to particle erosion in the second pattern. The quantitative relationship between the fine particles loss, the volumetric strain and the four influencing factors (i.e. time, hydraulic pressure, consolidated stress ratio and void ratio) are investigated using regression analysis based on 81 numerical simulations, respectively. The flow paths of the eroded fine particles are also investigated during the erosion process, which demonstrates that flow paths change alternatively between the blocked state and the opening state and then more flow paths in the model will open as the erosion process carries on.

Keywords: Seepage erosion; silty sand; fluid dynamics; discrete element; tunnel

1. Introduction

For shield driven tunnels assembled with segmental lining built in saturated soils, the tunnel convergence and differential longitudinal settlements may induce the opening and dislocation of segmental joints. Therefore, tunnel leakage frequently occurs through circumferential and longitudinal segmental joints. In low permeability soils, the tunnel leakage provides a new drainage boundary which will cause the decrease of pore pressure around the tunnel, and thus results in ground and tunnel settlements. The leakage-induced ground and tunnel responses can be significant in saturated fine soils and have been of great concern in tunnel engineering (O'Reilly et al., 1991;Yi et al., 1993; Mair & Taylor, 1997; Cooper et al., 2002; Shin et al., 2002; Asakura & Kojima, 2003; Wongsaroj et al., 2007; Mair, 2008; Zhang et al., 2012; Shen et al., 2014; Wu et al., 2015a, 2015b, 2016; Zhang et al., 2015; Xu et al., 2016). The common understanding on the effect of tunnel leakage on high permeable soil, for example sand and silty sand, is that it would not significantly reduce the pore pressure and would not induce ground or tunnel settlements. However, fine particles could be easily eroded by water seepage into the tunnel through the segmental joints because of the low cohesive force between the particles in sand or silty sand (see Fig. 1). This erosion of fine particles may result in the ground loss around the tunnel and increase the void ratio of the soil. The excessive ground loss will induce longitudinal differential settlements, which will reduce the stability of shield tunnels and then deteriorate the serviceability of tunnels. The erosion-induced increase of void ratio will seriously reduce the strength and stiffness of the soils around tunnel (Yin et al., 2014, 2016a), which will further induce settlements under external loads (e.g. traffic loading of subway). However, up to now the seepage erosion induced hazards have been mainly studied for earth dams (Wan & Fell, 2004; Fox, 2006; Richards, 2007; Chang & Yin, 2011; Midgley, 2013; Yin et al., 2016b). More attention should be paid to the tunnel engineering.

Previous studies of erosion mainly focused on dam engineering. The grain size distribution (GSD), the confining pressure and the hydraulic pressure, as well as the size of the soils constriction affect the erosion process. For example, Kenny (1986) suggested an H-F geometrical curve to distinguish the stable grading from the unstable grading for particle erosion; Tomlinson (2000) presented that high confining pressure can also produce significant particle erosion because high confining pressure can break the arching bridges formed by the fine particles across the inter-particle voids and result in more erodible fine particles; the constriction size, defined as the size of narrow voids along the flow path which is the key obstacle for fine particles to travel successfully through the flow path, is another important factor affecting the particle erosion. The constriction size distribution was found to be closely related to the GSD, material relative density and the cumulative amount of eroded fine particles (Indraratna, 2007; Reboul, 2010).

Compared with earth dams, the characteristic of particle erosion around tunnels are as follows: (1) the soil particles are subjected to various confining and axial pressures depending on the tunnel embedded depth; (2) the erosion boundary is specific because particle erosion happens only through the seams of tunnel segmental joints. For silty sand foundation, the various confining and axial pressures are always associated with various void ratios along the depth. Therefore, the void ratio is used to characterize the stress states in this paper. Besides, under different hydraulic pressure and consolidated stress ratio, silty sand can have different performance during the erosion process. Furthermore, time is another important factor to define the erosion process. All these factors deeply influence the seepage erosion process around shield tunnel and these processes need to be clarified. Among many ways, the coupling CFD-DEM should be an effective method ~~with foundamentals of physics~~ which can provide insights of fundamental physics.

DEM appears to be promising for investigating the seepage erosion process coupled with

CFD, particularly the migration and erosion of fine particles (Zhao & Shan, 2013; Sibille et al., 2015). DEM treats soils as an assembly of discrete particles. It starts with the basic constitutive laws at inter-particle contacts at microscopic scale and develops into the responses of the particle assembly under different loading conditions at the macroscopic scale. The advantage of DEM lies in that it can physically capture the behavior of particulate materials, and as a discontinuous analysis method it can simulate the large deformation and discontinuous process of discrete particle assembly under quasi-static and dynamic condition (see Jiang & Yin, 2012, 2014; Jiang et al., 2016). Therefore, it can potentially overcome the shortcomings of the finite element method and is a powerful numerical tool for computing the motion of large number of particles in the large deformation and discontinuous analyses of particle eroding. However, few investigations by CFD-DEM simulating the seepage erosion process in granular materials around shield tunnels have been conducted up to now.

The main objectives of this paper are: (1) to investigate the seepage erosion mechanism of soils around tunnels under various stress states and hydraulic pressures, and (2) to obtain the quantitative relationship between the fine particles loss, the volumetric strain and the four influencing factors: time, hydraulic pressure, consolidated stress ratio and void ratio. For this, the extensive CFD-DEM modelling of erosion is performed under various influencing factors. The confining and axial pressures applied on the DEM model are used to simulate the stress states of the soils around shield tunnels. In this paper, three stress states are applied on the DEM model to generate three void ratios of soil models representing loose, medium dense and dense silty sand, respectively. The specific erosion boundary of longitudinal and circumferential segmental joints is simulated using the perpendicular erosion seams at the bottom plate. The seepage erosion mechanism under various stress states and the specific erosion boundary is interpreted.

2. Numerical simulations

2.1 Description of CFD-DEM

The CFD option for PFC 3D enables the combination of the DEM calculation with the computational fluid dynamics model (Itasca Consultant Group, 2003). In this paper, the CFD solves the incompressible Navier-Stokes equation on a 3D discretized fluid cell consisting of mapped hexahedra grid as shown in Fig.4(c). In each fluid cell, the fluid force acting on each particle is calculated and assigned based on the fluid conditions in the fluid cell that the particle occupies. The presence of particles in each fluid cell is accounted by the porosity terms in the fluid equation including the Navier-Stokes equation and the continuity equation.

The Navier-Stokes equation can be modified to include the effect of a particulate solid phase into the fluid. Since the average effects over many particles are focused on (as opposed to attempting to model the details of fluid flow between particles), they can be characterized in terms of porosity n and a coupling force f_b, as show in the Eq. (1).

$$\rho_f \frac{\partial v}{\partial t} + \rho_f \frac{v}{n} \cdot \nabla(v) = -n\nabla p + \mu \nabla^2(v) + f_b \tag{1}$$

where ρ_f is the density of the fluid, p is the fluid pressure, μ is the dynamic viscosity of the fluid, v is the Darcy fluid velocity.

The Darcy fluid velocity can be calculated by the Darcy's law using Eq.(2).

$$v = ki = k\frac{\Delta P}{\gamma_w l} \tag{2}$$

where i is the hydraulic gradient, P is the hydraulic pressure, γ_{w} is the unit weight of water, l is the length of the flow path which is the height of soil model in this study, k is the permeability (or hydraulic conductivity coefficient) of soil with units of length over time.

The permeability can be calculated according to the Kozeny-Carman relation using Eq.(3).

$$k = \frac{\gamma_w}{\mu_f} B \frac{n^3}{(1-n)^2} d^2 \qquad (3)$$

where μ_f is the dynamic fluid viscosity in Pa·s, B is a geometric factor taken as 1/180, d is the grain diameter. According to Eq.(3), the value of k of models in this study ranges from 1.317×10^{-6}m/s to 2.880×10^{-5}m/s for different void ratios.

The drag force per unit volume applied by the particles to the fluid in each fluid element is defined as

$$f_b = \beta(u-v) \qquad (4)$$

where β is an empirical parameter. According to Tsuji (1993), the parameter β can be calculated in one of two ways, depending on the porosity of the fluid element. For high values of porosity ($n\geq0.8$), β is derived from the corrected nonlinear drag force exerted on a spherical particle by a fluid relating to the Reynolds number. For low values of porosity ($n<0.8$), β is derived from the Ergun relations (see Ergun 1952) as shown in Eq.(5). In this study, the porosity is lower than 0.8.

$$\beta = \frac{(1-n)}{d^2 n^2}(150(1-n)\mu_f + 1.75\rho_f d(u-v)) \qquad (5)$$

where d is the average diameter of particles in the fluid element.

The drag force f_{drag} is the body force experienced by the fluid as a result of moving particles. A force equal and opposite is distributed to the particles in each fluid element, which is proportional to the volume of each particle, defined as fluid drag force, f_{drag}.

$$f_{drag} = \frac{4}{3}\pi r^3 \frac{f_b}{1-n} = \frac{4}{3}\pi r^3 \beta(v-u)(1+e) \qquad (6)$$

where r is the particle radius, e is the void ratio.

The coupling between the CFD and DEM in each time step is volume-averaged and two-way, which means that the force acting on the particles in one fluid cell is also applied to the fluid as an average over the same fluid cell. The total fluid drag force is determined in PFC and divided by the volume of the fluid cell in CFD. The CFD determines the fluid velocity and fluid pressure gradient in each fluid cell. So in each time step when the coupling information are exchanged, PFC sends CFD the current porosity and the total fluid drag force. At the same time CFD sends PFC the current fluid velocity and fluid pressure gradient in each fluid cell. After that, the PFC program runs forward one time step for given interval seconds when the fluid drag force and porosity in each fluid cell are recalculated. Then the PFC program moves to the next time step.

The DEM code of PFC 3D was used to build the soil models. The inter-particle contact and the particle-wall contact in normal and tangential directions were modelled by the linear contact model proposed by Cundall (1979) as shown in Fig. 2. The contacts in normal and tangential directions contain a spring to resist the inter-particle force and a dashpot that allows energy dissipation and quasi-static deformation. A divider is set in the normal and tangential directions so that the contact force can be reset to zero if the two particles are separated. A slider is set in the tangential direction to provide shear force controlled by the Coulomb friction between two contact particles.

The instantaneous transitional and angular accelerations can be calculated based on the Newton's 2nd Law using the contact force and moment applied on each particle. The position and the force state of each soil particle can be recorded at each time step. By generating tens of thousands of soil particles, the erosion process can be simulated with recording its deformation.

2.2 Simulation process

2.1.1 Grain size distribution

In order to have an axisymmetric condition which can reduce the particle number compared to cubic DEM model, ~~T~~the cylindrical DEM model was designed with 0.7 mm in diameter and 0.7 mm in height within the CFD domain. It contains about twenty thousand particles with six different diameters as shown in Fig. 3. The grain size distribution (GSD) follows the gap-graded pattern proposed by Wan and Robin (2004) which was widely used to study the erosion related issues. In Fig. 3, the dashed line represents the on-site GSD of Shanghai silty sand around tunnels, and the solid line represents the gap-graded GSD in the model. The simplified gap-graded GSD represents the main characteristic of the GSD of on-site soil. The width of the erosion seam is 0.1 mm. So the gap-graded GSD is simplified as two categories of coarse particles and fine particles. For coarse particles, the diameters are between 0.25 mm to 0.1 mm, and for the fine particles, the diameters are between 0.025 mm to 0.0125 mm. The transitional particles with diameters ranging from 0.1 mm to 0.025 mm were ignored because they can hardly pass the constrictions formed by the coarse particles with the maximum diameter of 0.25 mm. The particles with diameters smaller than 0.0125 mm were also ignored, since minor effects could be induced by these too fine particles with computational demand.

The coarse particles form the skeleton force chain in the model and they can not be eroded through the erosion seam. The fine particles are erodible and the erosion of fine particles will induce re-arrangement of particles and their skeleton force chain, thus result in volumetric strain of the model. So the simplified GSD represents the main characteristic of the GSD of on-site soil and ignores the minor one to save the computational time.

2.1.2 Model preparation

The model preparation followed four steps. First, the homogeneous model was generated using the Multi-layer Method according to Jiang & Yin (2012, 2014), as shown in Fig. 4(a). The model was generated by three layers in this step. The first layer was in the bottom and particles were randomly generated in this layer. The axial pressure was then applied on the top wall to compress the first layer, while the confining pressure was applied on the lateral wall to keep the lateral walls still. The axial and confining pressures were gradually applied to the target value as presented in Table 1. The target pressures can be determined corresponding to the on-site pressures around the tunnel. This process was repeated for the second and third layers until the model was fully generated. Along this way, three types of DEM models (Model-1, Model-2 and Model-3) were generated by applying three stress states of confining and axial pressures and the corresponding void ratios were 0.14, 0.31 and 0.43, representing dense, medium dense and loose sand respectively, as presented in Table 1.

Then, the model was consolidated under target confining and axial pressures as presented in Table 1. In the deposition process, an efficient servo-control algorithm coded based on the manual from the Itasca Consulting Group (2003) was used to keep the confining and axial pressures constant and to save the computational time.

Afterwards, the perpendicular seams with the width of 0.1 mm were generated at the bottom of the model as shown in Fig. 4(b), through which the fine particles would be gradually eroded by seepage. The perpendicular seams were used to simulate the perpendicular longitudinal and conferential joints of segmental tunnel lining.

Finally, the hydraulic pressure was applied using the fluid cell (Shimizu, 2004; Ravichandran, 2010). The 3×3×3 grids of fluid cell were used and shown in Fig. 4(c). If the size of the grid is too small, singularity in the governing equations of the fluid may happen when one coarse particle occupies one fluid cell and reduces the porosity of the fluid cell to nearly zero. Since the diameter of the coarse particle is larger than 0.2 mm and the height of the soil model is 0.7 mm, the 3×3×3 grids of fluid cell were used to avoid the computational singularity.

2.1.3 Seepage erosion progress

After the completion of DEM model, the seepage erosion progress was started and particles migration was triggered. Both the axial pressure and hydraulic pressure caused the fine particles erosion. Particles near the seams at the bottom were firstly pushed out of the model by the axial pressure. And soon, particle arch formed above the seams and stopped further erosion. Afterwards, further erosion occurred due to the fluid drag force induced by the differential hydraulic pressure. A single particle will lose the balance and start migrating following certain erosion paths when subjected to the fluid drag force. Correspondingly, in shield tunnel engineering, when the opening and dislocation of the segmental joints develop large enough for particles passing through, the fine particles will flow into the tunnel from the segmental joints. This process is repeating up to a stable state.

Different values of hydraulic pressure were used as shown in Table 1 to study its influence on the seepage erosion.

2.3 Model Parameters

The parameters for soil particle, wall cell and fluid cell are presented in Table 2. For the soil particle, a granular density of 2650 kg/m^3 and a friction coefficient of 0.3 were used based on previous studies (Jiang & Yin, 2012, 2014). The normal and shear stiffnesses were calibrated from the macro-parameters of the Shanghai silty sand by trial and error tests according to Luo (2007). Note that the unit of stiffness for spherical particles is “pa” instead of “N/m” in two-dimensional discs, and in this study the particle stiffness is constant and independent of the particle radius (Itasca Consulting Group, 2003). For the wall cell, the normal and shear stiffnesses were set to be 10 times bigger than the particle stiffness to prevent the particles from passing through the walls. The parameters of the fluid cell were derived based on the behaviour of pure water under the pressure of 100 kPa and the temperature of 20℃.

3. Progression of seepage erosion

3.1 Seepage erosion-induced fine particles loss

The fine particles loss was defined as the mass ratio of the eroded fine particles to all particles in the model, which can be distinguished by the axial pressure extruding induced fines loss and the hydraulic pressure induced fines erosion. For instance, when the head pressure is 0, the particle loss is only generated by the axial compression extrusion, which can be defined as the Case 1 (pure extrusion); when the head pressure is increased to 100 kPa keeping other conditions the same, the particle loss is caused by the axial compression as well as the drag force due to seepage, which can be defined as Case 2. Then, the amount of particle loss caused only by the seepage drag force is equal to the Case 2 minus Case 1.

The progression of fine particles loss with time for all three models under the same hydraulic pressure of 100kPa was presented in Fig. 5(a) with results under no applied hydraulic pressure (0 kPa) shown in Fig. 5(b) as a reference. For the Model-1 with dense sand, the progression of erosion-induced fine particles loss can be divided into two stages so-called as the extruding-eroding coupled stage and the eroding-dominated stage. In the former, the fine particles loss increases rapidly with time during which an important part of fines loss (up to around t = 1s when the increasing rate becomes small and stable shown in Fig. 5(b)) is ~~and it is mainly~~ induced by axial pressure extruding particles through the erosion seam on the bottom. In the latter, the increase of fine particles loss with time slows down and the fine particles loss gradually reaches stable, during which fine particles loss is mainly induced by the fluid drag force dragging particles to the bottom of the model. The fine particles loss for medium dense sand by Model-2 and loose sand by Model-3 keeps increasing in the eroding-dominated stage at different paces. The fine particles loss of the Model-3 is most significant during the progression of seepage erosion.

The fine particles loss at a reference time of seepage erosion was defined as the reference fine particles loss. Note that the reference time of seepage erosion is set at t=6s which is enough for the comparison with saving computational time. The reference fine particles loss of the three models under different hydraulic pressures was presented in Fig. 5(~~b~~c). The exponential relation was found between the reference fine particles loss and the hydraulic pressure. The interception on the *w* axis is the reference fine particles loss corresponding to the null hydraulic pressure, which is caused by the axial pressure squeezing the fine particles passing through the bottom seams. As interpreted in the former section, the axial pressure-induced fine particles loss is the first pattern of erosion. The axial pressure-induced reference fine particles loss for Model-1, Model-2 and Model-3 are 1.1%, 0.69% and 0.49% respectively. Further erosion is prevented by the particle-arch formed above the seam. It is larger for the dense sand Model-1 than for the loose sand Model-3 because the axial pressure applied on the Model-1 is larger than that on the on Model-3. When the hydraulic pressure was applied, the reference fine particles loss increases with the hydraulic pressure because the fluid drag force is applied on each particle. However, the increasing rate for the dense sand Model-1 is much slower than the loose sand Model-3. For instance, when the hydraulic pressure increased from 0 to 100 kPa, the reference fine particles loss for the loose sand Model-3 increased from 0.49% to 5.8% while the reference fine particles loss for the dense sand Model-1 only increased from 1.1% to 1.67%. This implies that for dense sand, the reference fine particles loss is mainly induced by the axial pressure. Whilst, for loose sand the reference fine particles loss is mainly induced by the hydraulic pressure. Generally, the axial pressure results in more fine particles loss for dense sand than for loose sand, while the hydraulic pressure results in more fine particles loss for loose sand than for dense sand. The combined reference fine particle loss caused by axial pressure and hydraulic pressure is more important for loose sand and less important for dense sand.

The coupling effect of void ratio and hydraulic pressure on the reference fine particles loss is illustrated in Fig. 6, which indicates that the coupling of high void ratio and high hydraulic pressure results in the very significant reference fine particles loss of 14%.

3.2 Seepage erosion-induced volumetric strain

In the models, force chains are formed in the granular materials to resist axial and confining pressures. The force chains are composed of coarse particles and part of fine particles. Particles erosion results in particles re-arrangement in the force chains, and thus leads to volumetric strain of the model.

Fig. 7(a) shows the evolution of the volumetric strain with time under the same hydraulic pressure of 100 kPa for three models. The evolution of volumetric strain can also be divided into two stages: extruding stage and eroding stage. During the extruding stage, the volumetric strain increases rapidly. Then, the increasing of volumetric strain slows down with time and the volumetric strain gradually reaches a stable state at the end of the eroding stage. However, for the medium dense sand Model-2, the volumetric strain in the eroding stage increases slowly. This will be explained in the section 4 of this paper in terms of the flow path in medium dense sand Model-2 later on.

The volumetric strain at the reference time of seepage erosion was defined as the reference volumetric strain. Fig. 7(b) shows the reference volumetric strain of the three models under different hydraulic pressures. The linear correlation was found between the reference volumetric strain and the hydraulic pressure. The interception on the ε_v axis is the reference volumetric strain with null hydraulic pressure and is induced by the axial pressure. The axial pressure-induced reference volumetric strain for Model-1, Model-2 and Model-3 are 1.27%, 1.33% and 0.93% respectively. It is larger for the dense sand Model-1 than for the loose sand Model-3, which implies that the axial pressure introduces more volumetric strain for dense sand than for loose sand. But the differences between the three models are not obvious. Under the hydraulic pressure, the volumetric strain of the loose sand Model-3 increases faster than that of the dense sand Model-1. When the hydraulic pressure increased from 0 to 100 kPa, the reference fine particles loss for the Model-3 increased from 0.93% to 1.2% (0.27% increased), while the reference fine particles loss for the Model-1 increased from 1.27% to 1.4% (0.13% increased). It implies that the hydraulic pressure produces more volumetric strain for loose sand than for dense sand. This is in consistency with the progression of reference fine particles loss described in the previous section. However, the hydraulic pressure-induced increasement of volumetric strain is not obvious compared to axial pressure-induced volumetric strain. This implies that the axial pressure plays the major role for volumetric strain in both dense and loose sand. Besides, under the same hydraulic pressure, the reference fine particles loss is more important for loose sand Model-3 as shown in Fig. 5(~~b~~c), while the reference volumetric strain is less important for loose sand Model-3 as shown in Fig. 7(b). This is because that the fine particles loss is defined as the mass ratio of the eroded fine particles to all particles of the model, and the total mass of Model-1 is much bigger than Model-3 which gives a smaller ratio, even though the mass of eroded fine particles in Model-1 surpasses that of Model-3.

Comparing Fig. 5(a) with Fig. 7(a), for loose sand Model-3, about 85% of the reference volumetric strain with only 32% of the reference fine particles loss happened in the extruding stage. In the eroding stage, the volumetric strain reaches stability while the fine particle loss keeps increasing. It means that further particle loss in this stage does not increase the volumetric strain any more. These particles can be defined as the floating particles as shown in Fig. 8. The erosion of skeleton particles will directly lead to the increase of volumetric strain. Whilst, the erosion of floating particles will only increase the voids between the skeleton force chains and isolate the skeleton particles from each other. The isolated skeleton force chains in loose sand Model-3 are able to balance the static forces but with less resistance to the dynamic traffic loading. Once the force chains collapse under the dynamic traffic loading, further volumetric strain will develop. So the erosion of floating particles in the eroding stage increases the risk of further volumetric strains under cyclic traffic loading in shield tunnels.

For dense sand Model-1, about 90% of the reference volumetric strain with 72% of the reference fine particles loss happened in the extruding stage. In the eroding stage, both the volumetric strain and fine particles loss reach a stable state. There are two reasons leading to this phenomenon. First, the mass ratio of floating particles in dense sand model is smaller than that in loose sand model. Secondly, particles in the dense sand Model-1 are less likely to be hollowed out by fluid drag force compared with loose sand Model-3.

The coupling effect of void ratio and hydraulic pressure on the volumetric strain is illustrated in Fig. 9. It shows that high hydraulic pressure coupled with high void ratio results in a larger volumetric strain. The maximum volumetric strain in Fig. 9 can be as large as 2.5%, which could cause additional damage to the tunnel lining.

4. Flow path analysis

The flow path was recorded to investigate the particle movements under the hydraulic pressure. In the model, the erodible fine particles are dragged by the fluid drag force following many possible flow paths among the skeleton force chains. Each flow path has a constriction with the minimum diameter which may stuck the fine particles. Tracing the fine particles can record the flow path in 3D coordinate system.

The positions of the particles were monitored every 750 steps and recorded by the coordinates. The flow path can be then obtained by connecting the monitored positions. Dense points on the flow path imply that the particle is blocked for a relatively long time, whereas loose points on the flow path imply that the particle is unobstructed.

Fig. 10 shows the flow path of two eroded particles. The origin of coordinate is at the bottom center of the model. The coordinate for the top center of the model is (0,0,0.7). The fine particle with the ID of 28968 is blocked at the height of 0.3 mm temporarily. The fine particle with the ID of 26237 is blocked at the height of 0.5 mm temporarily. These two flow paths closed during the period that the fine particles were blocked and then re-opened when the constriction hole gets enlarged due to the movement of the force chain. And the fine particles continued moving until they met the next blocking condition or got out of the model from the perpendicular seams at the bottom. Fig. 11 shows the flow paths of two fine particles blocked at the height of 0.1 mm and 0.4 mm respectively. These two flow paths were not re-opened untill the end of the simulation.

During the erosion process, the erodible fine particles always find the least energy consuming path among many other paths. The erosion process can be described using three modes as shown in Fig. 12. Mode 1 is shown in Fig. 12(a), where the fine particle is smaller than the constriction hole so that the particle can go through without consuming extra energy. During this process, the volumetric strain did not develop. Mode 2 is shown in Fig. 12(b), where a fine particle was blocked at the constriction hole and the path was closed temporarily. Fine particles blocked around the entrance of the path have to find other least energy consuming paths to go through. Mode 3 is shown in Fig. 12(c), where the skeleton force chain formed by the coarse particles was removed by the unbalanced force due to particle re-arrangement. The constriction hole was enlarged and the previous blocked fine particles could go through again. This is why fine particles with IDs of 28968 and 26237 continue migrating after temporary obstruction. The three modes of erosion can appear separately or alternatively.

The modes of flow path described in Fig. 12 are only for an individual one. The real flow paths in the model consist of thousands of such individual flow paths, which form a complex flow net. Since it is very difficult to describe the flow net directly, the distribution of flow paths was described by analysing the variation of numbers of fine particles in different layer of the studied model.

Each model was equally divided into three layers, denoted as top, middle and bottom layer along its height. Fig. 13(a) shows the fine particle distribution with time for different layers of Model-3 under the hydraulic pressure of 100 kPa. For Model-3, the amount of fine particles in the top layer decreases with time, whereas the number of fine particles in the middle and bottom layers is unchanged with time. It implies that the eroded fine particles flow through the top, middle and bottom layers successively. So the particles flow process follows the mode 1 of erosion as shown in Fig. 12(a). This can explain that the loose sand Model-3 experienced most significant fine particle loss but results in least significant volumetric strain among the three models.

For Model-2 in Fig. 13(b), the number of fine particles in the top and bottom layers decreases with time during the extruding stage and the eroding stage, whereas the number of fine particles in the middle layer increases with time during the extruding stage and reaches a stable state during the eroding stage. It indicates that during the extruding stage, the flow paths from middle layer to bottom layer closed so that the fine particles from the top layer were blocked in the middle layer. Whereas in the eroding stage, the paths are re-opened so that the number of fine particles in the middle layer tends to stabilize. For the medium dense sand Model-2, the particle flow in each layer follows different flow mode. The re-opening of the flow path in the eroding stage results in the increase of the volumetric strain as shown in Fig. 7(b).

For Model-1 in Fig. 13(c), the number of fine particles in bottom layer decreases with time, whereas the number of fine particles in the top and middle layers remains unchanged. It indicates that most of the flow paths from the top layer to the bottom layer were blocked. Fine particles near the perpendicular seams at the bottom layer were eroded until the particle arch is formed and the further erosion is prevented. This can explain the evolution of volumetric strain with hydraulic pressure as shown in Fig. 7 (b). Most of the volumetric strain was caused by the axial pressure rather than hydraulic pressure.

From the above analysis, the develpoment of the flow paths can be described in different layers without portraying the complex and unpredictable flow network in the model.

5. Regression analysis

In order to obtain the quantitative relationship between the reference fine particles loss, the volumetric strain and the influencing variables, a regression analysis was conducted based on the numerical results. The influencing variables were considered in this study are: 1) time t; 2) hydraulic pressure P_u; 3) consolidation stress ratio K_0; and 4) void ratio e. To eliminate the influence of dimensions in the regression analysis, the time t and hydraulic pressure P_u were normalized by two reference parameters t_0 and P_0 , where t_0 is 1 second and P_0 is the confining pressure listed in Table 1. The upper and lower bounds for the influencing variables are listed in Table 3. The specific value for each variable was given between the upper and lower bounds. For t/t_0, it has been given 9 values of 0.2, 0.4, 0.6, 0.8, 1, 2, 3, 4, 5. Five values were given from 0 to 1 because the fine particles loss and the volumetric strain increase significantly during this period of extruding stage of seepage erosion. For the other three variables, the values are averagely set between the upper and lower bounds.

The amount of DEM simulation can be 9×5×6×5=1350 if fully combining the four variables. Therefore, the principle of orthogonal experiment was used for the four variables to optimize the simulation, based on which 81 simulations were carried out after optimization using the orthogonal combination (Zhang et al. 2015; Kung et al. 2007).

The variations of averaged fine particles loss w and volumetric strain ε_v with the influencing variables are presented from Fig. 14 to Fig. 17, in which the averaged values of w and ε_v were obtained by taking the arithmetic average of w and ε_v at a certain value of the influencing variable. For example, using 18 simulations with K_0 =0.75 presented in Table 4, the averaged values of w and ε_v were obtained by taking the arithmetic average of w and ε_v values. Along this way, the averaged values of w and ε_v corresponding to various influencing variables can be obtained using the same method.

The averaged w with the four variables is presented in Fig. 14. The averaged w varies nonlinearly with each normalized variable. These nonlinear trends can be empirically fitted by an exponential or a power function with a coefficient of determination (R^2) higher than 0.75. Based on the four best fitted curves in Fig. 14, a function can be established to interpret the systematic variation of w with the four normalized variables as

$$w = e^{a_0} \times e^{a_1 \ln(t/t_0)} \times e^{a_2/K_0} \times e^{a_3 \ln(P_u/P_0)} \times e^{a_4/e} \tag{7}$$

where w is the fine particle loss. a_i are the function coefficients. Taking the logarithm scale for both sides of Eq. (7), a multi-linear function can be obtained as

$$\ln w = a_0 + a_1 \ln\left(\frac{t}{t_0}\right) + \frac{a_2}{K_0} + a_3 \ln\left(\frac{P_u}{P_0}\right) + \frac{a_4}{e} \tag{8}$$

Then, the multiple linear regression analysis can be carried out using Statistical Product and Service Solutions (SPSS). Eq. (8) was used to fit all data from 81 simulations. The best-fitted function coefficients are listed in Table 5. Eq. (8) associated with these coefficients has the R^2 of 0.87.

Similarly, the averaged ε_v with four variables is presented in Fig. 15. The nonlinear trend of averaged ε_v with each variable can be empirically fitted by an exponential or a power function. The function of ε_v is established as

$$\varepsilon_v = e^{b_0} \times e^{b_1 \ln(t/t_0)} \times e^{b_2/K_0} \times e^{b_3 \ln(P_u/P_0)} \times e^{b_4 e^2 + b_5 e} \tag{9}$$

$$\ln \varepsilon_v = b_0 + b_1 \ln\left(\frac{t}{t_0}\right) + \frac{b_2}{K_0} + b_3 \ln\left(\frac{P_u}{P_0}\right) + b_4 e^2 + b_5 e \tag{10}$$

where, ε_v is volumetric strain, b_i are function coefficients.

The function coefficients in Eq. (10) can also be obtained by conducting multiple linear regression analysis. The function coefficients are listed in Table 6. Eq. (10) associated with these coefficients has the R^2 of 0.64.

Thus, the quantitative function between the averaged w and ε_v and the four influencing variables were obtained. It is worth noting that Eq. (8) and Eq. (10) should be limited within the range of values discussed in this study.

Comparing Fig. 14 and Fig. 15, the evolution tendency for fine particles loss and volumetric strain with the first three variables is similar. Both fine particles loss and volumetric strain increase with time t/t_0 and hydraulic pressure P_u/P_0 and decrease with consolidation stress ratio K_0. But the tendency for the last variable (void ratio e) is opposite. This is because the variation of fine particles loss and volumetric strain is caused by axial pressure and hydraulic pressure, as explained in the former section. From Fig. 14(d), the contribution of these two factors can be separated into Fig. 16(a) adding Fig. 16(b), which shows the evolution of averaged fine particles loss with void ratio by axial pressure and hydraulic pressure respectively. And similarly, Fig. 15(d) can be separated into Fig. 17(a) and Fig. 17(b) which shows the evolution of averaged volumetric strain with void ratio by axial pressure and hydraulic pressure respectively.

The separated evolutions for fine particles loss and volumetric strain are similar in Fig. 16 and Fig. 17. This similar evolution tendency shows that the dense sand is more prone to particle erosion caused by axial pressure, and loose sand is more prone to particle erosion caused by hydraulic pressure. But the variation rate of fine particles loss is always faster than volumetric strain. This conclusion is in consistency with the conclusion in the former section.

6. Conclusions

The mechanism of seepage erosion around shield tunnels was investigated for dense, medium dense and loose silty sand using CFD-DEM coupling simulations. The gap-graded GSD of soil particles was used in all simulations. Different confining pressure, axial pressure and hydraulic pressure were applied on the soil model to simulate different stress sate of the soils around shield tunnel in saturated silty sand foundation. The opening and dislocation of tunnel segmental joints were modelled by the perpendicular erosion seam in the bottom of the model. The erosion process was studied in terms of the evolutions of fine particles loss and volumetric strain for dense, medium dense and loose sand, respectively. The findings are summarized as follows:

(1) The erosion of fine particles around tunnels is caused by axial and hydraulic pressures. Particles near the seams at the bottom are firstly extruded through the seams by the axial pressure. Further erosion is caused by fluid drag force due to hydraulic pressure.

(2) For loose sand, fine particles loss is mainly induced by fluid drag force. While for dense sand, fine particles loss is mainly induced by axial pressure. The combined fine particle loss caused by axial pressure and hydraulic pressure is most for loose sand and least for dense sand.

(3) For the volumetric strain of both dense and loose sand, the axial pressure plays the major role with the fluid drag force due to hydraulic pressure playing the minor role. Under the hydraulic pressure, the volumetric strain of loose sand increases relatively faster than dense sand. Thus under low hydraulic pressure, the volumetric strain for dense sand is more pronounced than loose sand. But the volumetric strain of loose sand can surpass that of dense sand under high hydraulic pressure.

(4) The major role of fluid drag force is to migrate the fine particles between the skeleton force chains and isolate the skeleton particles from each other, thus reducing the resistance to the dynamic traffic loading. The minor role of fluid drag force is that when particle migration changes the skeleton force chain and enlarges the flow path, it will also lead to the increase of volumetric strain.

(5) The erodible fine particles always find the least energy consuming path among many other paths during migration. Loose sand has more unblocked flow paths than dense sand. More flow paths will open during the erosion process and the change of flow path is always accompanied with the increase of volumetric strain.

(6) Two quantitative relations between the two objective variables of w, ε_v and the four

influencing variables of t/t_0, K_0, P_u/P_0, e were obtained by regression analysis. They can be used to predict the variation tendency of w and ε_v under different conditions.

Acknowledgment

This study was substantially supported by the Natural Science Foundation of China (No. 41772295, 51478344, 51579179), the Shanghai Science and Technology Committee (No. 16DZ1200403).

References:

1. Asakura, T., Kojima, Y., 2003. Tunnel maintenance in Japan. Tunnelling and Underground Space Technology, 18(2–3), 161-169.

2. Chang, C. S., Yin, Z. Y., 2011. Micromechanical modeling for behavior of silty sand with influence of fine content. International Journal of Solids & Structures, 48(19), 2655-2667.

3. Wan, C. F., Robin, F., 2004. Investigation of Rate of Erosion of Soils in Embankment Dams. Journal of geotechnical and geoenvironmental engineering, 130(4), 373-380.

4. Cooper, M. L., Chapman, D. N., Rogers, C. D. F., Chan, A. H. C., 2002. Movements in the Piccadilly Line tunnels due to the Heathrow Express construction. Géotechnique, 52(4), 243-257.

5. Ergun, S., 1952. Fluid Flow through Packed Columns. Chemical Engineering Progress, 48(2), 89-94.

6. Fox, G. A., Wilson, G. V., 2006. Sediment Transport Model for Seepage Erosion of Streambank Sediment. Journal of Hydrologic Engineering, 11(6), 603-611.

7. Itasca Consultant Group, 2003. Particle Flow Code in 3 Dimensions Online Manual Version 3.0. Minneapolis, Minnesota. Itasca Consulting Group Inc.

8. Indraratna, B., Raut, A. K., Khabbaz, H., 2007. Constriction-based retention criterion for granular filter design. Journal of geotechnical and geoenvironmental engineering, 133(3), 266-276.

9. Jiang, M.J., Yin, Z.Y., 2012. Analysis of stress redistribution in soil and earth pressure on tunnel lining using the discrete element method. Tunnelling and Underground Space Technology, 32(6), 251-259.

10. Jiang, M.J., Yin, Z. Y., 2014. Influence of soil conditioning on ground deformation during longitudinal tunneling. Comptes Rendus Mécanique, 342(3), 189-197.

11. Jiang, M. J., Leroueil, S., Konrad, J. M., 2004. Insight into shear strength functions of unsaturated granulates by DEM analyses. Computers and Geotechnics, 31(6), 473-489.

12. Jiang, M. J., Yan, H. B., Zhu, H. H., Utili, S., 2011. Modeling shear behavior and strain localization in cemented sands by two-dimensional distinct element method analyses. Computers and Geotechnics, 38(1), 14-29.

13. Kenney, T. C., Lau, D., 1986. Internal stability of granular filters. Canadian Geotechnical Journal, 23(1), 215–225.

14. Kung, G. T. C., Juang, C. H., Hsiao, E. C. L., Hashash, Y. M. A., 2007. Simplified model for wall deflection and ground-surface settlement caused by braced excavation in clays. Journal of geotechnical and geoenvironmental engineering, 133(6), 731-747.

15. Mair, R. J., 2008. Tunnelling and geotechnics: new horizons. Géotechnique, 58(9), 695-736.

16. Mair, R. J., Taylor, R. N., 1997. Theme lecture: Bored tunneling in the urban environment. Paper presented at the Proceedings of the Fourteenth International Conference on Soil Mechanics and Foundation Engineering.

17. Midgley, T. L., Fox, G. A., Wilson, G. V., 2013. Seepage-induced streambank erosion and instability: in situ constant-head experiments. Journal of Hydrologic Engineering, 18(10), 1200-1210.

18. O'Reilly, M. P., Mair, R. J., Alderman, G. H., 1992. Long-term settlements over tunnels: an eleven-year study at Grimsby. International Journal of Rock Mechanics and Mining Sciences, 29(2), A96.

19. Ravichandran, N., Machmer, B., Krishnapillai, H., Meguro, K., 2010. Micro-scale modeling of saturated sandy soil behavior subjected to cyclic loading. Soil Dynamics and Earthquake Engineering, 30(11), 1212-1225.

20. Reboul, N., Vincens, E., Cambou, B., 2010. A computational procedure to assess the distribution of constriction sizes for an assembly of spheres. Computers and Geotechnics, 37(1-2), 195-206.

21. Richards, K. S., Reddy, K. R., 2007. Critical appraisal of piping phenomena in earth dams. Bulletin of Engineering Geology and the Environment, 66(4), 381-402.

22. Shimizu, Y., Hart, R. D., Cundall, P. A., 2004. Fluid Coupling in PFC2D and PFC3D. Paper presented at the Proceedings of the 2nd International PFC Symposium, Kyoto, Japan.

23. Shin, J. H., Addenbrooke, T. I., Potts, D. M., 2002. A numerical study of the effect of groundwater movement on long-term tunnel behaviour. Géotechnique, 52(6), 391-403.

24. Sibille, L., Lomine, F., Poullain, P., Sail, Y., Marot, D., 2015. Internal erosion in granular media: direct numerical simulations and energy interpretation. Hydrological Processes, 29(9), 2149-2163.

25. Shen, S. L., Wu, H. N., Cui, Y. J., Yin, Z. Y., 2014. Long-term settlement behavior of the metro tunnel in Shanghai, Tunneling and Underground Space Technology, 40(12), 309-323.

26. Tomlinson, S. S., Vaid, Y., 2000. Seepage forces and confining pressure effects on piping erosion. Canadian Geotechnical Journal, 37(1), 1-13.

27. Tsuji, Y., 1993. Disceret Particle Simulation of Two-Dimensional Fluidized Bed., Powder Technology, 77, 79-87.

28. Luo, Y., 2007. Simulation of soil mechanical behaviors using discrete element method based on particle flow code and its application. Ph.D. thesis, Zhejiang Univ. Zhejiang, China (in Chinese).

29. Wongsaroj, J., Soga, K., Mair, R. J., 2007. Modelling of long-term ground response to tunnelling under St James's Park, London. Géotechnique, 57(1), 75-90.

30. Wu, Y. X., Shen, S. L., Yuan, D. J., 2016. Characteristics of dewatering induced drawdown curve under barrier effect of retaining wall in aquifer, Journal of Hydrology, 539, 554-566.

31. Wu, H. N., Shen, S. L., Ma, L., Yin, Z. Y., Horpibulsuk, S., 2015. Evaluation of the strength increase of marine clay under staged embankment loading: a case study, Marine Georesources and Geotechnology, 33(6), 532-541.

32. Wu, H. N., Shen, S. L., Liao, S. M., Yin, Z. Y., 2015. Longitudinal structural modelling of shield tunnels considering shearing dislocation between segmental rings, Tunneling and Underground Space Technology, 50, 317-323.

33. Xu, Y. S., Shen, S. L., Ren, D. J., Wu, H. N., 2016. Factor analysis of land subsidence in Shanghai: a view based on Strategic Environmental Assessment, Sustainability, 8(6), 573-585.

34. Yi, X., Rowe, R. K., Lee, K. M., 1995. Observed and calculated pore pressure and deformations induced by an earth balance shield. Canadian Geotechnical Journal, 32(1), 190-191.

35. Yin, Z.Y., Huang, H. W., Hicher, P.Y., 2016. Elastoplastic modeling of sand-silt mixtures. Soils and Foundations, 56(3), 520-532.

36. Yin, Z. Y., Hicher, P. Y., Dano, C., Jin, Y. F., 2016. Modeling Mechanical Behavior of Very Coarse Granular Materials. Journal of Engineering Mechanics, C4016006.

37. Yin, Z. Y., Zhao, J., Hicher, P. Y., 2014. A micromechanics-based model for sand-silt mixtures. International Journal of Solids & Structures, 51(6), 1350-1363.

38. Zhang, D. M., Ma, L. X., Huang, H. W., Zhang, J., 2012. Predicting Leakage-induced Settlement of Shield tunnels in Saturated Clay. Cmes-Computer Modeling in Engineering & Sciences, 89(3), 163-188.

39. Zhang, D. M., Phoon, K. K., Huang, H. W., Hu, Q. F., 2015. Characterization of Model Uncertainty for Cantilever Deflections in Undrained Clay. Journal of geotechnical and geoenvironmental engineering, 141(1), 04014088.

40. Zhang, N, Shen, S. L., Wu, H.N., Chai, J.C., Yin, Z.Y., 2015. Evaluation of effect of basal geotextile reinforcement under embankment loading on soft marine deposits, Geotextiles and Geomembranes, 43(6), 506-514.

41. Zhang, G., 2007. Researches on meso-scale mechanism of piping failure by means of model test and PFC numerical simulation. Ph.D. thesis, Tongji Univ. Shanghai, China (in Chinese)

42. Zhou, J., Yao, Z. X., Zhang, G., 2007. Mesomechanical simulation of seepage flow in sandy soil. Chinese Journal of Geotechnical Engineering, 29(7), 977-981 (in Chinese).

43. Zhao, J., Shan, T., 2013. Coupled CFD-DEM simulation of fluid-particle interaction in geomechanics. Powder Technology, 248–258.

Tables

Table 1 Pressures applied on the soil models

Model No.	Model-1				Model-2				Model-3			
Confining pressure(kPa)	3000				250				130			
Axial pressure(kPa)	4000				360				210			
Hydraulic pressure(kPa)	500	250	100	50	180	100	50	22.5	100	50	25	10
Void ratio	0.14				0.31				0.43			

Table 2 Parameters for soil particles and fluid

	Granular density ρ(kg/m^3)	Normal stiffness K_n (Pa)	Shear stiffness K_s (Pa)	Friction coefficient f_c	Fluid density (kg/m^3)	Dynamic viscosity (Pa·s)
Soil particle	2650	5e6	5e6	0.3	-	-
Wall cell	-	5e7	5e7	0.3	-	-
Fluid cell	-	-	-	-	998.23	1×10-3

Table 3 Upper and lower bounds of influencing variables and magnitude of specific value for each variable

Influencing variables	Upper and lower limits	Number of specific values
t/t_0	0-5	9
K_0	0.6-1.0	5
P_u/P_0	0.0-1.2	6
e	0.14-0.43	5

Table 4 Value of the variables corresponding to K_0=0.75

No.	K_0	t/t_0	P_u/P_0	e	ε_v (%)	w (%)
1	0.75	0.4	0.2	0.37	0.81	0.63
2	0.75	0.6	0.4	0.43	0.83	0.95
3	0.75	0.2	0.4	0.22	0.85	0.65
4	0.75	0.2	0.2	0.22	0.86	0.54
5	0.75	0.6	0.6	0.37	0.88	1.12
6	0.75	2	0.6	0.43	0.97	1.75
7	0.75	0.8	0.4	0.22	1.05	1.17
8	0.75	0.8	0.8	0.16	1.13	1.50
9	0.75	0.4	0.6	0.31	1.15	0.84
10	0.75	3	0.2	0.22	1.20	1.67
11	0.75	1	0.2	0.31	1.23	0.95
12	0.75	5	0.4	0.37	1.24	2.62
13	0.75	1	1.2	0.31	1.29	1.66
14	0.75	4	0.6	0.37	1.37	2.64
15	0.75	2	1	0.16	1.44	1.75
16	0.75	3	1	0.16	1.46	1.81
17	0.75	5	1.2	0.16	1.55	1.97
18	0.75	4	0.8	0.31	1.74	2.81
			averaged value		1.17	1.50

Table 5 Coefficients in the regression equation for *w*

Coefficients	Values
a_0	-0.148
a_1	0.391
a_2	0.426
a_3	0.214
a_4	0.009
R^2	0.87

Table 6 Coefficients in the regression equation for ε_v

Coefficients	Values
b_0	-0.222
b_1	0.137
b_2	0.129
b_3	0.12
b_4	-7.397
b_5	3.197
R^2	0.64

Figure list:

Fig. 1 Schematic of seepage erosion around tunnels

Fig. 2 Contact model of two disks in DEM

Fig. 3 Grain size distribution (GSD) in the numerical simulation (gap-gradation)

Fig. 4 Simulation process

Fig. 5 Progression of fine particles loss for three types of models (A: Extruding stage; B: Eroding stage)

Fig. 6 Coupling effect of hydraulic pressure and void ratio on the reference fine particles loss

Fig. 7 Progression of volumetric strain for three types of models (A: Extruding stage; B: Eroding stage)

Fig. 8 Floating particles and skeleton particles in the soil model

Fig. 9 Coupling effect of hydraulic pressure and void ratio on the reference volumetric strain

Fig. 10 Flow path of the eroded particles

Fig. 11 Flow path of the blocked particles

Fig. 12 Three modes of particle erosion process

Fig. 13 Fine particle distribution in three layers for three models under the hydraulic pressure of 100kPa (A: Extruding stage; B: Eroding stage)

Fig. 14 Evolution of averaged fine particles loss with influencing variables: (a) time (t/t_0); (b) consolidation stress ratio (K_0); (c) hydraulic pressure-consolidation pressure (P_u/P_0); (d) void ratio

Fig. 15 Evolution of averaged volumetric strain with influencing variables: (a) time (t/t_0); (b) consolidation stress ratio (K_0); (c) hydraulic pressure-consolidation pressure (P_u/P_0); (d) void ratio (e)

Fig. 16 Evolution of averaged fine particles loss with void ratio: (a) caused by axial pressure (b) caused by hydraulic pressure

Fig. 17 Evolution of averaged volumetric strain with void ratio: (a) caused by axial pressure (b) caused by hydraulic pressure.

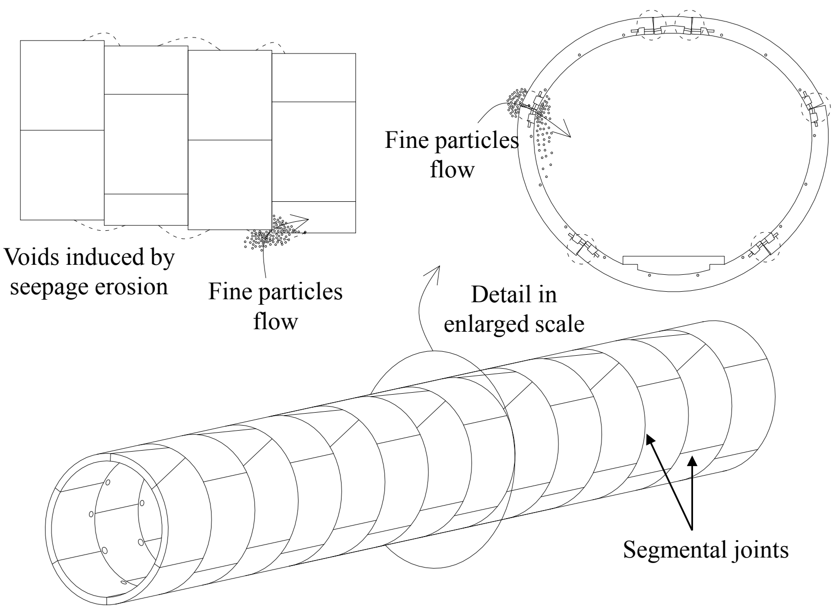

Fig. 1 Schematic of seepage erosion around tunnels

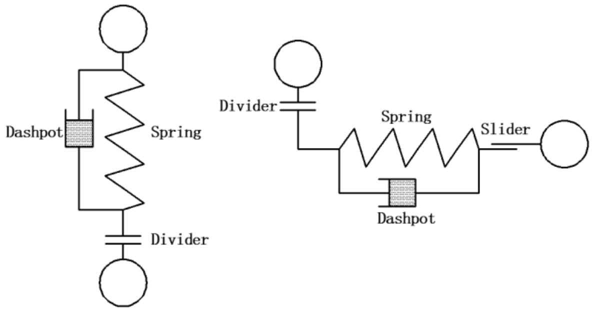

Fig. 2 Contact model of two disks in DEM

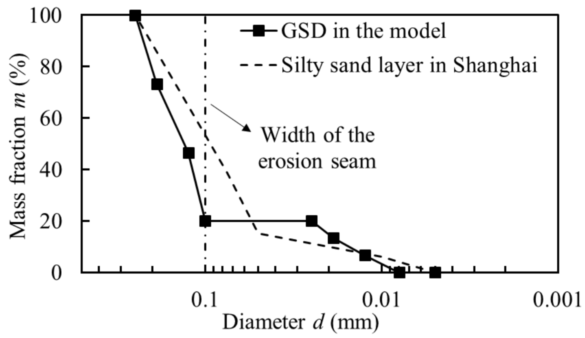

Fig. 3 Grain size distribution (GSD) in the numerical simulation (gap-gradation)

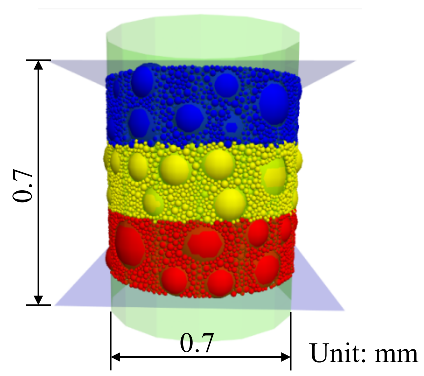

(a) Model generation

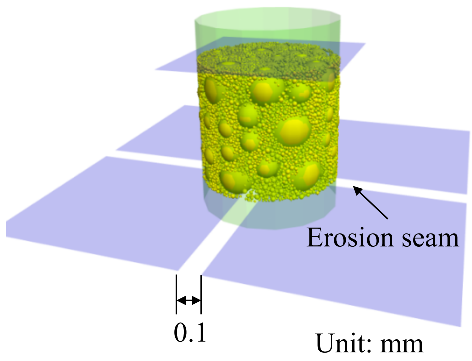

(b) Seam

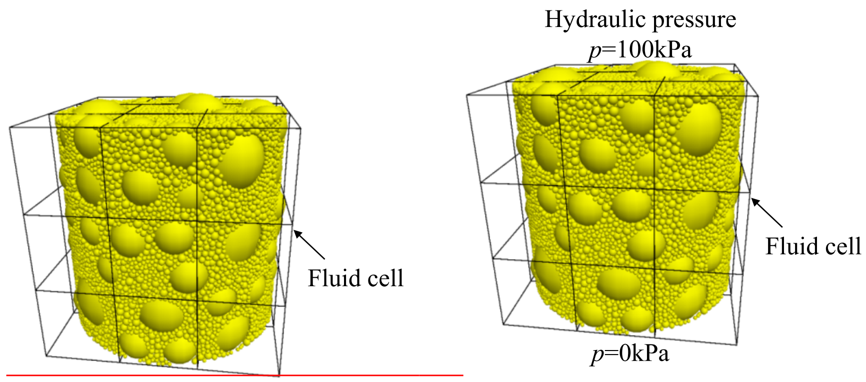

(c) Fluid cell under the hydraulic pressure of 100kPa

Fig. 4 Simulation process

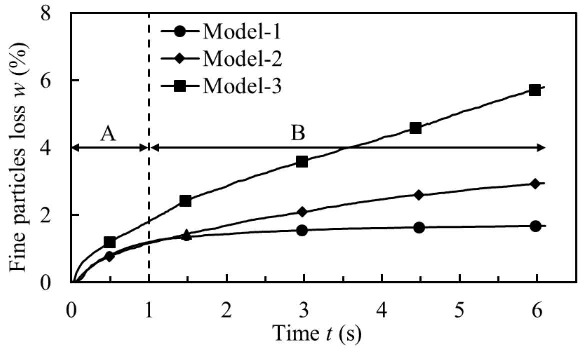

(a) Fine particle loss under the hydraulic pressure of 100 kPa

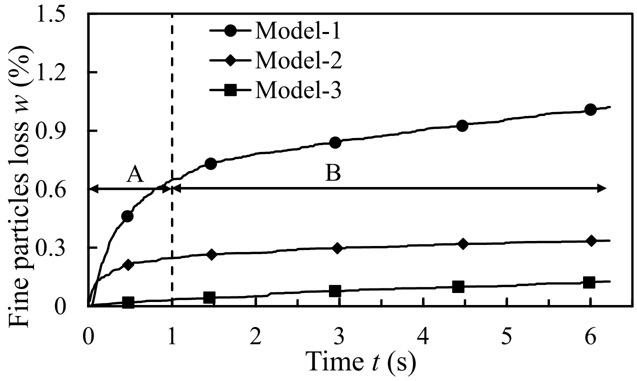

(b) Fine particle loss without hydraulic pressure (0 kPa)

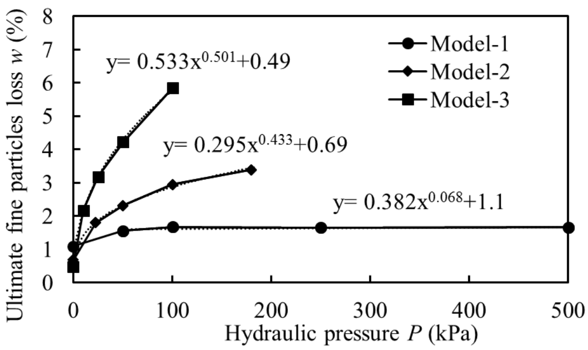

(~~b~~c) reference fine particles loss under various hydraulic pressures

Fig. 5 Progression of fine particles loss for three types of models (A: Extruding-Eroding coupled stage; B: Eroding-dominated stage)

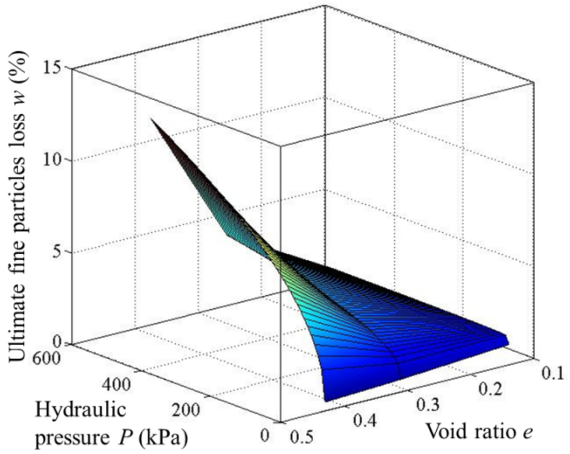

Fig. 6 Coupling effect of hydraulic pressure and void ratio on the reference fine particles loss

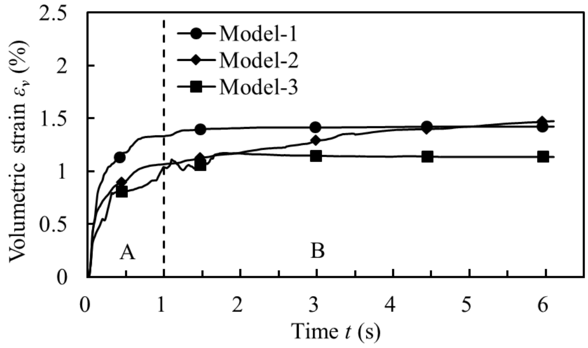

(a) Volumetric strain under the hydraulic pressure of 100 kPa

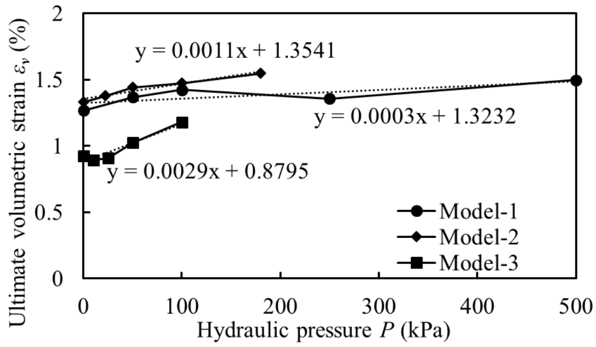

(b) reference volumetric strain under various hydraulic pressures

Fig. 7 Progression of volumetric strain for three types of models (A: Extruding stage; B: Eroding stage)

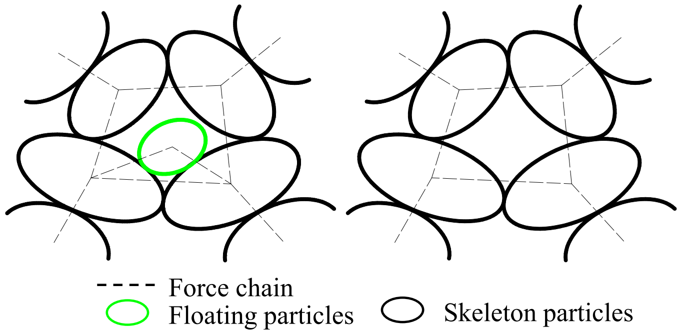

Fig. 8 Floating particles and skeleton particles in the soil model

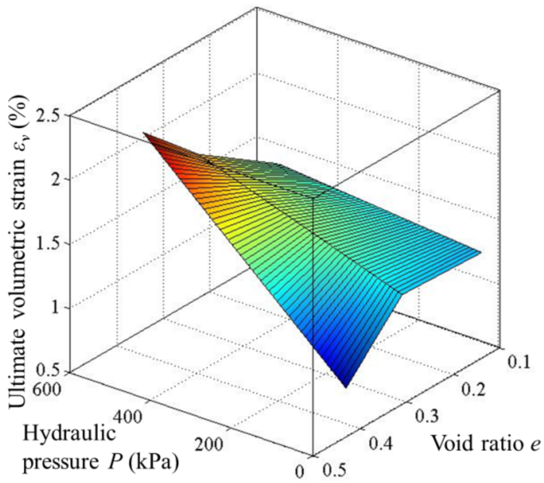

Fig. 9 Coupling effect of hydraulic pressure and void ratio on the reference volumetric strain

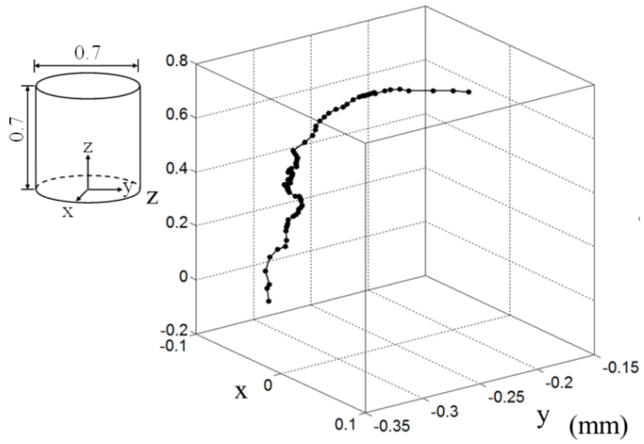

(a) Erosion path (particle id 28968)

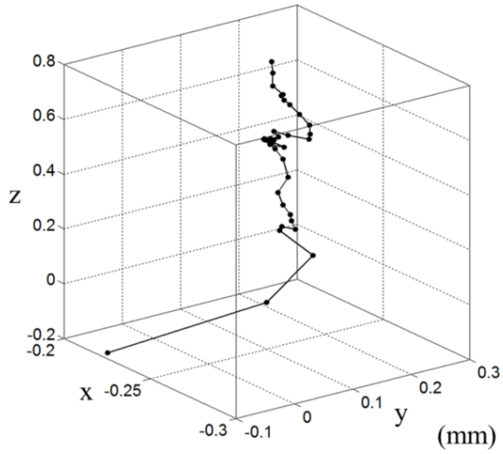

(b) Erosion path (particle id 26237)

Fig. 10 Flow path of the eroded particles

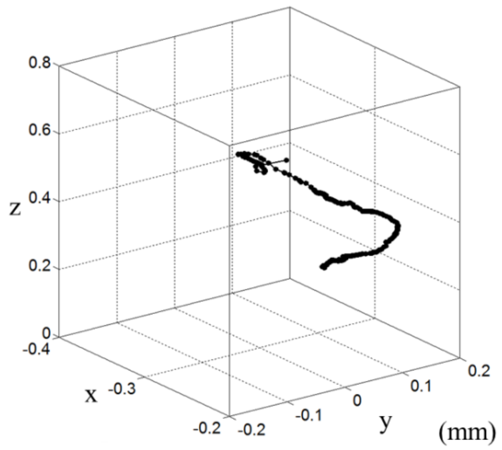

(a) Erosion path (particle id 26809)

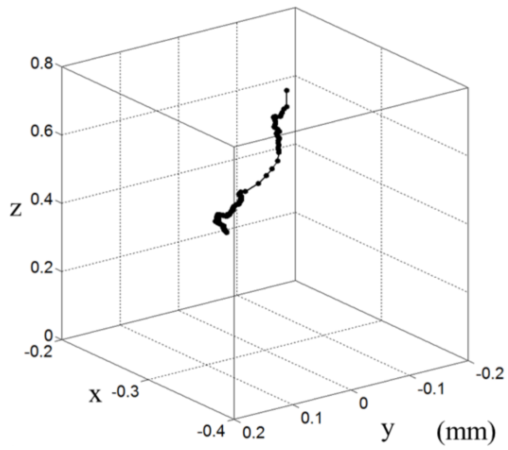

(b) Erosion path (particle id 26664)

Fig. 11 Flow path of the blocked particles

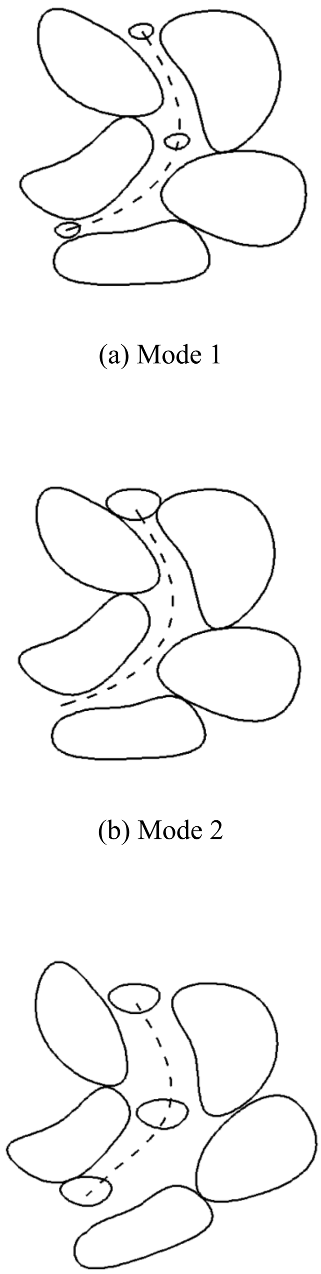

(a) Mode 1

(b) Mode 2

(c) Mode 3

Fig. 12 Three modes of particle erosion process

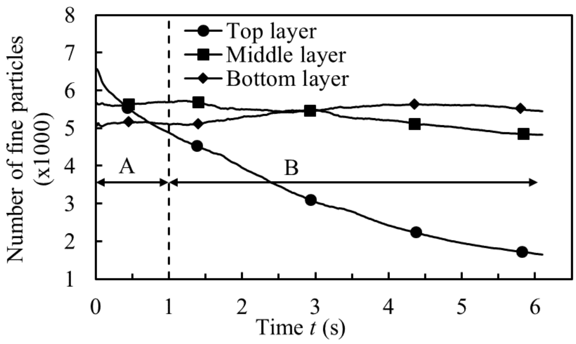

(a) Fine particles in each layer of Model-3

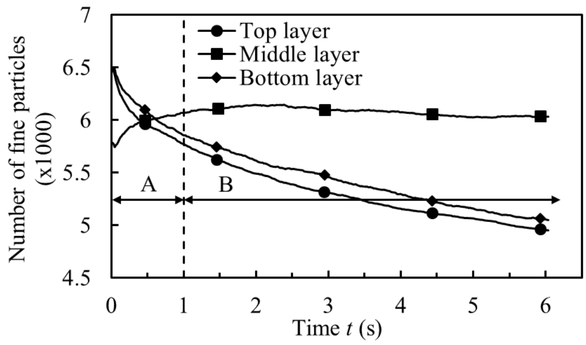

(b) Fine particles in each layer of Model-2

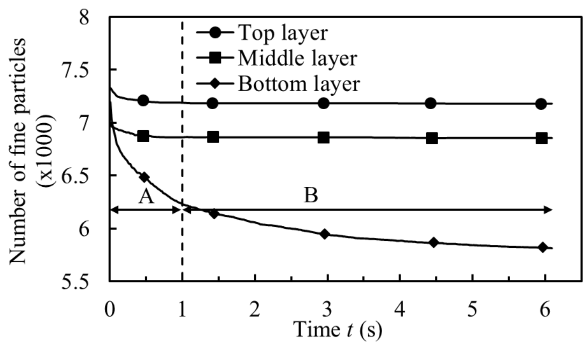

(c) Fine particles in each layer of Model-1

Fig. 13 Fine particle distribution in three layers for three models under the hydraulic pressure of 100kPa

(A: Extruding stage; B: Eroding stage)

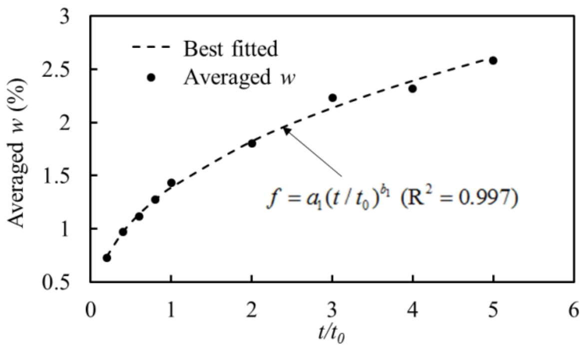
Best fitted
Averaged w
Averaged w (%)
$f = a_1(t/t_0)^{b_1}$ ($R^2 = 0.997$)
t/t0
0 1 2 3 4 5 6
0.5 1 1.5 2 2.5 3

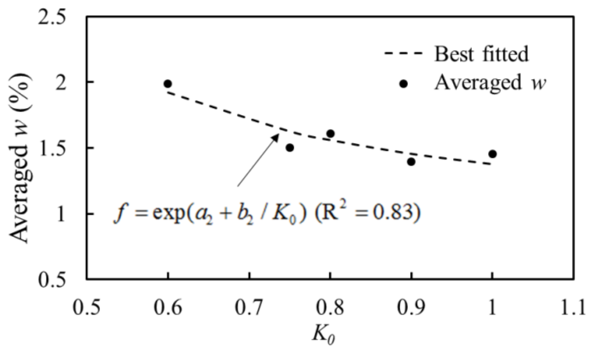
Best fitted
Averaged w
Averaged w (%)
$f = \exp(a_2 + b_2 / K_0)$ ($R^2 = 0.83$)
K0
0.5 0.6 0.7 0.8 0.9 1 1.1
0.5 1 1.5 2 2.5

(a) (b)

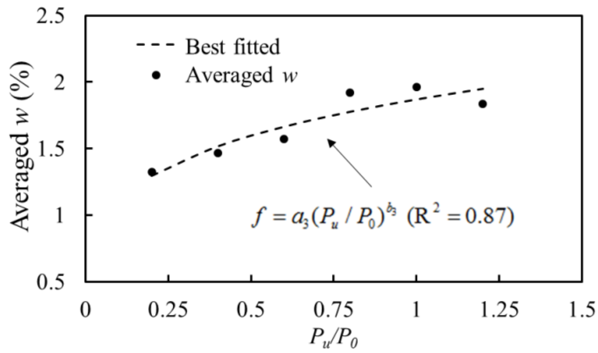
Best fitted
Averaged w
Averaged w (%)
$f = a_3(P_u / P_0)^{b_3}$ ($R^2 = 0.87$)
Pu/P0
0 0.25 0.5 0.75 1 1.25 1.5
0.5 1 1.5 2 2.5

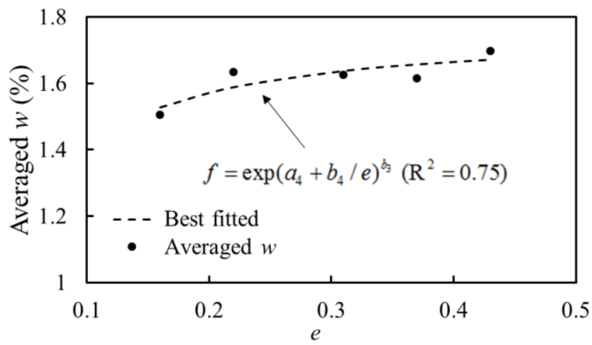
Best fitted
Averaged w
Averaged w (%)
$f = \exp(a_4 + b_4 / e)^{b_3}$ ($R^2 = 0.75$)
e
0.1 0.2 0.3 0.4 0.5
1 1.2 1.4 1.6 1.8

(c) (d)

Fig. 14 Evolution of averaged fine particles loss with influencing variables: (a) time (t/t_0); (b) consolidation stress ratio (K_0); (c) hydraulic pressure-consolidation pressure (P_u/P_0); (d) void ratio (e)

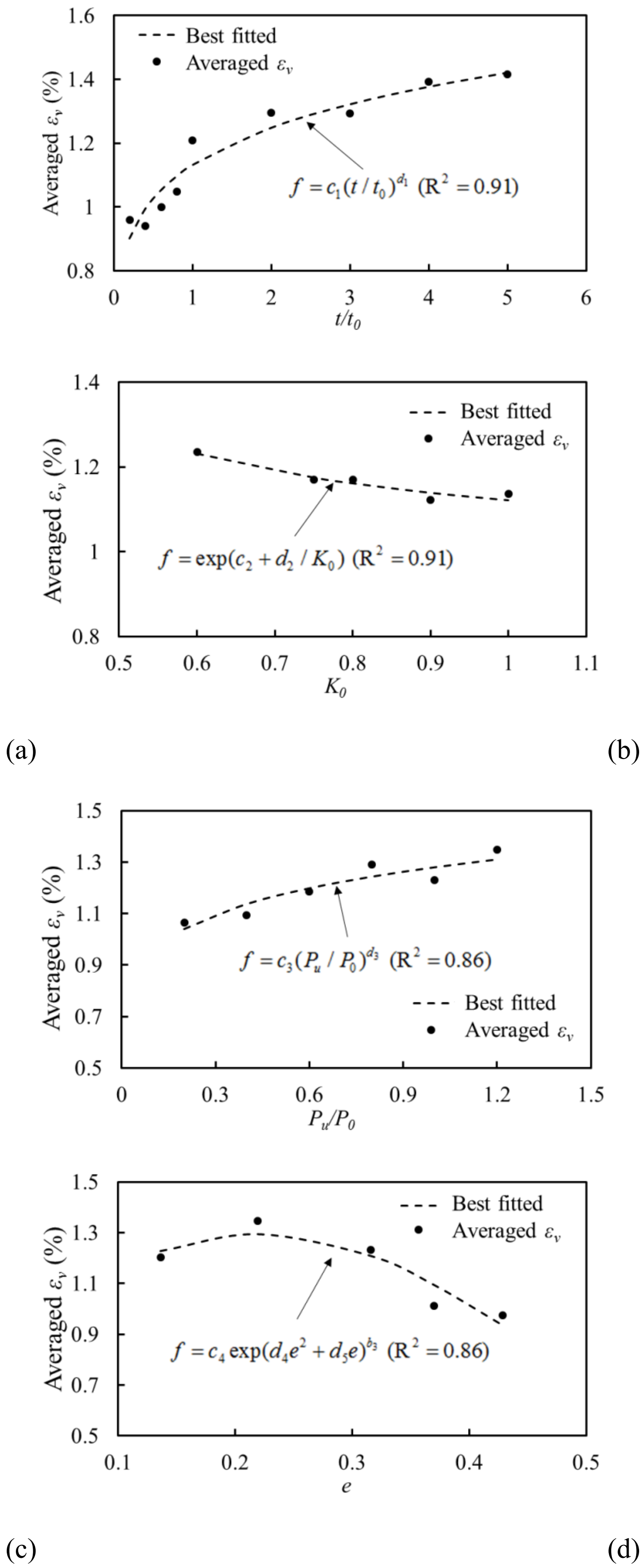

Fig. 15 Evolution of averaged volumetric strain with influencing variables: (a) time (t/t_0); (b) consolidation stress ratio (K_0); (c) hydraulic pressure-consolidation pressure (P_u/P_0); (d) void ratio (e)

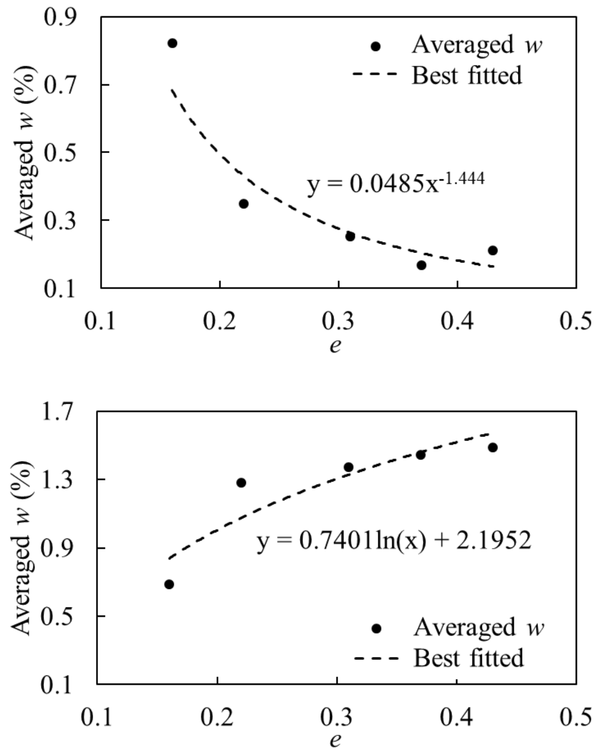

(a) (b)

Fig. 16 Evolution of averaged fine particles loss with void ratio: (a) caused by axial pressure (b) caused by hydraulic pressure

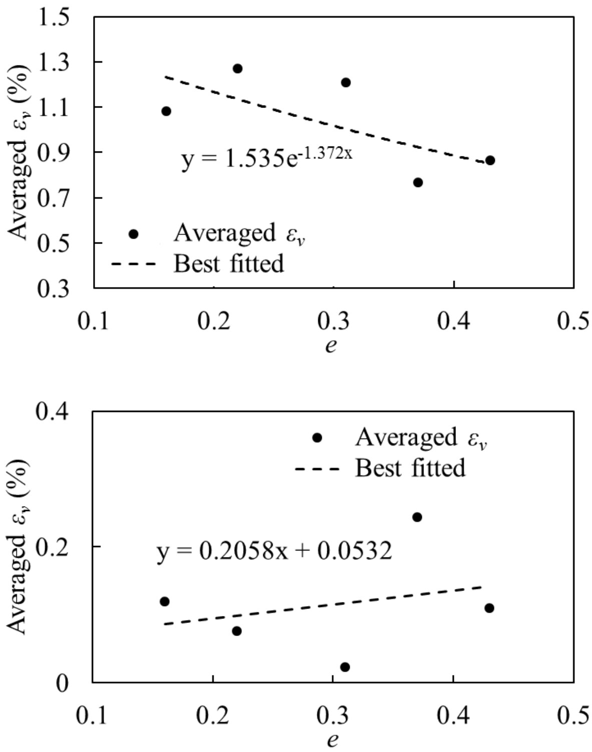

(a) (b)

Fig. 17 Evolution of averaged volumetric strain with void ratio: (a) caused by axial pressure (b) caused by hydraulic pressure